Gas Separation

International Edition: DOI: 10.1002/anie.202000323
German Edition: DOI: 10.1002/ange.202000323

Mixed Metal–Organic Framework with Multiple Binding Sites for Efficient C_2H_2/CO_2 Separation

Junkuo Gao, Xuefeng Qian, Rui-Biao Lin,* Rajamani Krishna, Hui Wu, Wei Zhou,* and Banglin Chen**

Abstract: *The separation of C_2H_2/CO_2 is particularly challenging owing to their similarities in physical properties and molecular sizes. Reported here is a mixed metal–organic framework (M′MOF), [Fe(pyz)Ni(CN)$_4$] (**FeNi-M′MOF**, pyz = pyrazine), with multiple functional sites and compact one-dimensional channels of about 4.0 Å for C_2H_2/CO_2 separation. This MOF shows not only a remarkable volumetric C_2H_2 uptake of 133 $cm^3\,cm^{-3}$, but also an excellent C_2H_2/CO_2 selectivity of 24 under ambient conditions, resulting in the second highest C_2H_2-capture amount of 4.54 $mol\,L^{-1}$, thus outperforming most previous benchmark materials. The separation performance of this material is driven by π–π stacking and multiple intermolecular interactions between C_2H_2 molecules and the binding sites of **FeNi-M′MOF**. This material can be facilely synthesized at room temperature and is water stable, highlighting **FeNi-M′MOF** as a promising material for C_2H_2/CO_2 separation.*

Metal–organic frameworks (MOFs) have emerged as very promising porous materials for adsorptive gas separation because they integrate the merits of tunable pore sizes and functional pore surfaces that can realize not only a molecular sieving effect, but also preferential gas binding.[1] Many MOFs have been explored for simplifying various gas separation and purification schemes ranging from mature ones, such as carbon dioxide capture (CO_2) from methane and nitrogen, to more challenging olefin/paraffin and alkyne/alkene separations.[2] For C_2H_2 and CO_2 gas molecules, the similarities in physical properties (differ in boiling point by ca. 3% and ca. 6 K) and identical molecular shapes/sizes (3.3 × 3.3 × 5.7 Å^3 for C_2H_2, 3.2 × 3.3 × 5.4 Å^3 for CO_2), with kinetic diameters of about 3.3 Å, make it very difficult and challenging to realize efficient porous materials for C_2H_2/CO_2 separation under ambient conditions.[3] A few ultra-microporous MOFs featuring bare oxygen or fluorine base sites have been developed to preferentially bind C_2H_2 molecules through hydrogen-bonding interactions or bind CO_2 molecules through electrostatic interactions, showing high C_2H_2/CO_2 selectivity but low C_2H_2 uptake.[4] Another approach is to incorporate strong adsorption binding sites, mainly open metal sites, into MOFs with large pore volumes to boost the uptake capacity of the preferred gas molecules.[5] **UTSA-74** represents a unique example with open metal centers having two accessible sites which can bind two C_2H_2 molecules, but only one CO_2 molecule, differing from its isomer **MOF-74** which adsorbs similar amounts of C_2H_2 and CO_2 under the same conditions.[5c] Though progress has been made over the past several years, the uptake capacity versus selectivity trade-off still poses a daunting challenge for addressing C_2H_2/CO_2 separation.[6]

The vast database of reported MOF structures enables comparative analyses to target potential candidates with dual functionalities, featuring moderate pore volumes and accessible functional sites, to realize both high gas uptake and separation selectivities. Among plentiful ligands, cyanide is a short and highly basic ligand that is feasible to construct robust MOFs with modest pore aperture size, such as Prussian blue and Hofmann-type compounds.[7] For those MOFs with metalloligands, the open metal sites on ligands are accessible for gas molecules, whereas expected narrow pore structures originating from compact ligands enforce additional multiple intermolecular interactions to form, as demonstrated by a series of mixed metal–organic frameworks (M′MOFs).[8] In this regard, a Hofmann-type MOF [Fe(pyz)Ni(CN)$_4$] (**FeNi-M′MOF**, pyz = pyrazine), discovered in 2001, showing open nickel sites and polarized surfaces as well as compact pore channels of about 4.0 Å, is particularly interesting.[9] The high density of functional sites and ultra-micropore would collaboratively enforce gas separation with high gas uptake and separation selectivities. Herein we investigate the mixed iron/nickel MOF **FeNi-M′MOF** for potential C_2H_2/CO_2 separation. In this MOF, C_2H_2 molecules are found to preferentially bind the organic moieties and open Ni sites through π–π stacking and multiple intermolecular interactions, respectively, whereas CO_2 molecules mainly distribute on the open Ni sites through relatively weak interactions. In this context, **FeNi-M′MOF** shows a very high C_2H_2/CO_2 selectivity of 24 that is superior to the previous top-perform-

---

[*] Prof. J. Gao, X. Qian
Institute of Functional Porous Materials, The Key laboratory of Advanced Textile Materials and Manufacturing Technology of Ministry of Education, School of Materials Science and Engineering, Zhejiang Sci-Tech University, Hangzhou 310018 (China)
E-mail: jkgao@zstu.edu.cn

Prof. J. Gao, Dr. R.-B. Lin, Prof. B. Chen
Department of Chemistry, University of Texas at San Antonio
One UTSA Circle, San Antonio, TX 78249-0698 (USA)
E-mail: ruibiao.lin@utsa.edu
banglin.chen@utsa.edu

Dr. R. Krishna
Van't Hoff Institute of Molecular Sciences, University of Amsterdam
Science Park 904, 1098 XH Amsterdam (The Netherlands)

Dr. H. Wu, Dr. W. Zhou
NIST Center for Neutron Research, National Institute of Standards and Technology, Gaithersburg, MD 20899-6102 (USA)
E-mail: wzhou@nist.gov

Supporting information and the ORCID identification number(s) for the author(s) of this article can be found under:
https://doi.org/10.1002/anie.202000323.

ing MOFs while retaining a remarkable C_2H_2 uptake capacity of 133 $cm^3\,cm^{-3}$, and thus an excellent C_2H_2-capture capacity of 4.54 $mol\,L^{-1}$ at 298 K and 1 bar for 50:50 C_2H_2/CO_2 separation, which is close to that of the benchmark UTSA-74 and exceeds that of other out-performing MOFs.[5c]

FeNi-M′MOF is a pillared-layer M′MOF, in which the $Fe[Ni(CN)_4]$ layer is connected by the pyz pillars. The Ni atoms show square-planar coordination geometry while Fe atoms are octahedrally coordinated. The Ni atoms are coordinated by carbon atoms of four different cyan groups, whereas the Fe atoms are fully coordinated by nitrogen atoms from four different cyan groups and two pyz linkers. $Fe[Ni(CN)_4]$ layers are then connected by pyz linkers into a three-dimensional network with one-dimensional channels of about 4.15 × 4.27 or 3.94 × 4.58 Å^2. The open metal site density of **FeNi-M′MOF** is about 9.2 $mmol\,cm^{-3}$, which is higher than that of most MOFs, as shown in Table S2 (see the Supporting Information).

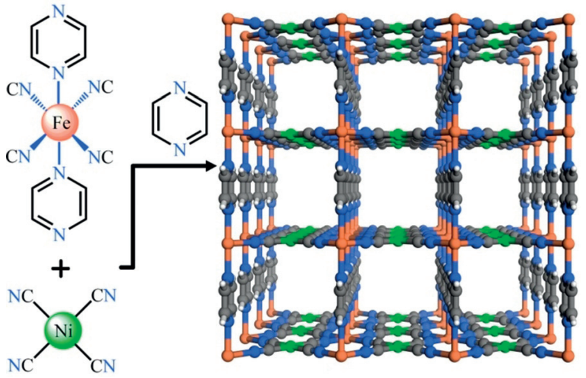

Figure 1. The crystal structure of **FeNi-M′MOF** viewed along the *a*/*b* axis. Fe, Ni, C, N, and H in **FeNi-M′MOF** are represented by orange, green, gray, blue, and white, respectively.

FeNi-M′MOF was synthesized at room temperature in water and methanol (Figure 1).[10] By adding the solution of $K_2[Ni(CN)_4]$ into the mixed methanol and water solution of Fe^{2+} and pyz, the **FeNi-M′MOF** microcrystalline powders were obtained after stirring for 30 minutes. The powder X-ray diffraction (PXRD) of products indicated that those products have a good crystallinity and match well with the simulated XRD pattern, indicating the purity of **FeNi-M′MOF**. The resultant **FeNi-M′MOF** was further validated by elemental analysis (EA), thermogravimetry analysis (TGA), energy dispersive spectroscopy (EDS), and X-ray photoelectron spectroscopy (XPS) analysis (see the Supporting Information). This MOF also exhibits excellent water stability as shown in Figure S2. After soaking in water for 30 days, the crystallinity of **FeNi-M′MOF** is still retained. The TGA curve indicated that **FeNi-M′MOF** exhibits a considerable thermal stability up to 200 °C (see Figure S4). The thermal stability of **FeNi-M′MOF** was also confirmed by variable-temperature PXRD (see Figure S5), indicating that **FeNi-M′MOF** can maintain its crystalline structure up to about 200 °C. The fast and facile synthesis method, excellent water stability, and good thermal stability indicate **FeNi-M′MOF** is a promising separation material for scale-up synthesis.

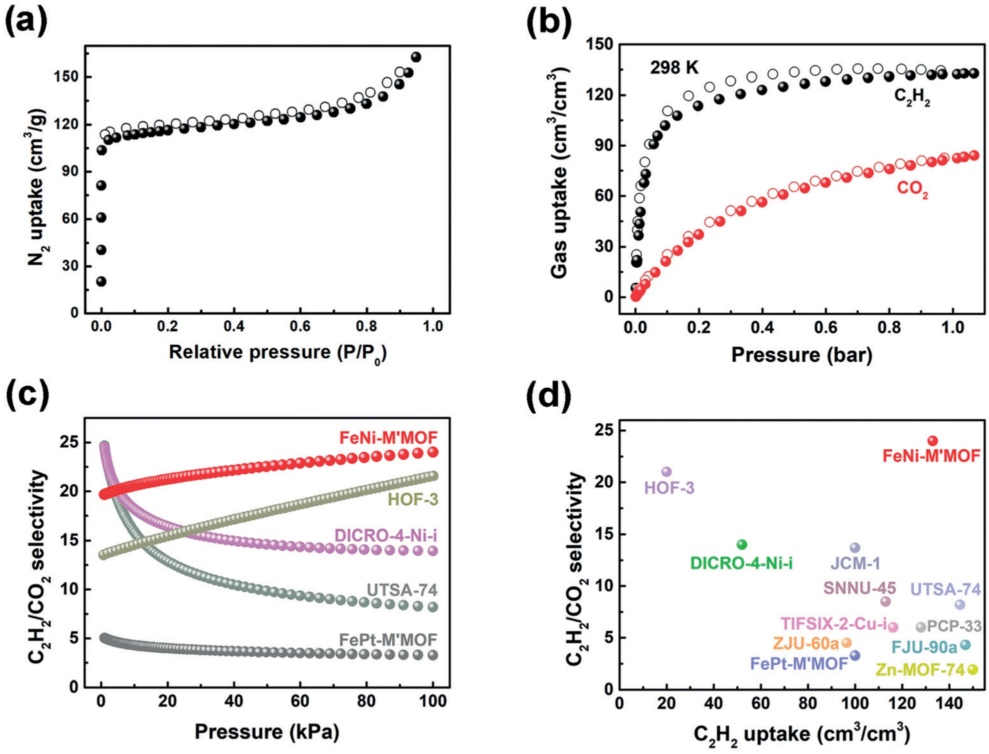

Figure 2. a) N_2 sorption isotherms for **FeNi-M′MOF** at 77 K. b) C_2H_2 and CO_2 sorption isotherms for **FeNi-M′MOF** at 298 K. c) Comparison of IAST selectivities for equimolar C_2H_2/CO_2 mixtures in **FeNi-M′MOF**, **FePt-M′MOF** and other materials in the range of 0–1 bar at 298 K. d) Comparison of C_2H_2/CO_2 adsorption selectivity and volumetric C_2H_2 uptake at 1 bar in **FeNi-M′MOF**, **FePt-M′MOF** and other porous materials.

The Brunauer-Emmett-Teller (BET) surface area of **FeNi-M′MOF** was measured to be 383 $m^2\,g^{-1}$ by an N_2 sorption experiment at 77 K as shown in Figure 2a. The experimental total pore volume is about 0.25 $cm^3\,g^{-1}$, and slightly smaller than the theoretical one calculated from the crystal structure (0.30 $cm^3\,g^{-1}$), which can be attributed to the insufficient filling of N_2 molecules in the ultramicroporous pore channels.

The C_2H_2 and CO_2 gas adsorption isotherms of **FeNi-M′MOF** were measured at both 273 and 298 K. As shown in Figure 2b, the volumetric C_2H_2 uptake capacity of **FeNi-M′MOF** is 133 $cm^3\,cm^{-3}$ (4.29 $mmol\,g^{-1}$) at 1 bar and 298 K, which is higher than those of many other MOFs, such as **DICRO-4-Ni-i** (52 $cm^3 cm^{-3}$),[4e] **ZJU-60a** (96 $cm^3 cm^{-3}$),[11] Cu[Ni(pdt)$_2$] (108 $cm^3 cm^{-3}$),[6a] **SNNU-45** (113 $cm^3 cm^{-3}$),[6b] **TIFSIX-2-Cu-i** (116 $cm^3 cm^{-3}$),[4f] **PCP-33** (128 $cm^3 cm^{-3}$),[12] and comparable to those of **UTSA-74** (144 $cm^3 cm^{-3}$),[5c] **FJU-90a** (146 $cm^3 cm^{-3}$),[6c] and **Zn-MOF-74** (150 $cm^3 cm^{-3}$).[13] The CO_2 uptake of **FeNi-M′MOF** is 84 $cm^3 cm^{-3}$ (2.72 $mmol g^{-1}$) at 1 bar and 298 K. At 1 bar and 273 K, C_2H_2 and CO_2 uptakes of **FeNi-M′MOF** are up to 145 and 102 $cm^3 cm^{-3}$ respectively, as shown in Figure S8. Interestingly, the Pt analogue [Fe(pyz)Pt(CN)$_4$] (**FePt-M′MOF**; see Figures S10–S12) shows much lower uptake capacities for C_2H_2 and CO_2 (100 and 105 $cm^3 cm^{-3}$, respectively), indicating the potential binding contribution of Ni sites in this type of MOF for C_2H_2 molecules. To evaluate the separation performance of this material, ideal adsorbed solution theory (IAST) was employed to calculate the adsorption selectivity. As shown in Figure 2c, at 100 kPa and 298 K, the C_2H_2/CO_2 (50:50) selectivity of **FeNi-M′MOF** is 24. The selectivity of **FeNi-M′MOF** is higher than those of most MOFs, such as **Zn-MOF-74** (1.92),[5c] **FJU-90a** (4.3),[6c] **UTSA-74a** (8.2),[5c] **JCM-1** (13.4),[4b] **DICRO-4-Ni-i** (13.9),[4e] and benchmark **HOF-3a** (21).[14] It should be noted that both the uptake capacity and separation selectivity can significantly affect the practical performance of an adsorbent. **HOF-3a** has a high selectivity, but the low uptake of C_2H_2 reduced its separation performance. In contrast, **FeNi-M′MOF** can address such trade-offs between the adsorption capacity and selectivity as shown in Figure 2d. The high selectivity and high C_2H_2 adsorption capacity of **FeNi-M′MOF** jointly reveal its useful separation potential for C_2H_2/CO_2.

Transient breakthrough simulations were conducted to demonstrate the C_2H_2/CO_2 separation performance of **FeNi-M′MOF**. The simulations in Figure 3a demonstrate the **FeNi-M′MOF** is of potential use for this challenging separation of C_2H_2/CO_2 mixtures. The C_2H_2/CO_2 mixtures (50:50) were used as feeds to mimic the industrial process conditions. Pure CO_2 first eluted through the bed, where the CO_2 purity was 99.95%, followed by the breakthrough of C_2H_2 after a certain time, τ_{break}, during which **FeNi-M′MOF** was saturated by C_2H_2. The C_2H_2-capture amount of **FeNi-M′MOF** is 4.54 $mol L^{-1}$ based on the simulated column breakthrough, which is close to that of the benchmark UTSA-74 (4.86 $mol L^{-1}$)[5c] and higher than those of most out-performing MOFs, such as **Zn-MOF-74** (4.06 $mol L^{-1}$),[5c] **FJU-90a** (4.16 $mol L^{-1}$),[6c] and **PCP-33** (4.16 $mol L^{-1}$).[12] Accordingly, **FeNi-M′MOF** shows not only a high C_2H_2/CO_2 selectivity and high C_2H_2 uptake but also high C_2H_2-capture capability from gas mixtures, endowing this material with a useful C_2H_2/CO_2 separation potential. Based on experimental breakthrough studies, we further evaluated the performance of **FeNi-M′MOF** in near practical separation processes for a C_2H_2/CO_2 mixture (50:50 v/v) as shown in Figure 3b. Indeed, **FeNi-M′MOF** exhibits excellent C_2H_2/CO_2 mixture separation performance at 298 K. CO_2 was first eluted through the adsorption bed without any detectable C_2H_2, whereas the latter was retained in the MOF column for a remarkable period prior to saturate the MOF. The retention time of pure CO_2 and C_2H_2 for C_2H_2/CO_2 (50:50 v/v) mixture on **FeNi-M′MOF** are up to 24 and 40 min, respectively. Accordingly, the captured C_2H_2 was calculated to be 4.10 $mol L^{-1}$ with a separation factor of 1.7.

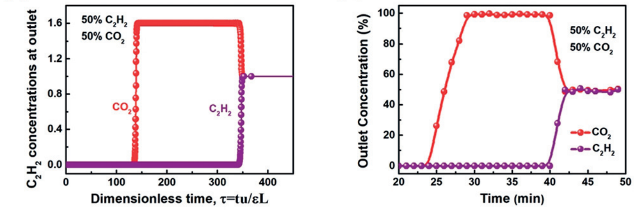

Figure 3. a) Transient breakthrough simulations for separation of equimolar C_2H_2/CO_2 mixture using **FeNi-M′MOF** at 298 K, with a partial pressure of 50 kPa for each. b) Experiment breakthrough curves for equimolar C_2H_2/CO_2 mixture in a packed column with **FeNi-M′MOF** at 298 K and 1 bar.

The isosteric heat of adsorption (Q_{st}) has been used to evaluate the strength of interaction between the adsorbent and the adsorbate, which is calculated (see Figure S13) from the adsorption isotherms at 273 and 298 K. The Q_{st} values are 27–32.8 and about 24.5 $kJ mol^{-1}$ of **FeNi-M′MOF** for C_2H_2 and CO_2, respectively. The Q_{st} value of C_2H_2 in **FeNi-M′MOF** is lower than those of other MOFs such as **HKUST-1** (39 $kJ mol^{-1}$),[15] **FeMOF-74** (47.5 $kJ mol^{-1}$),[16] and **SIFSIX-2-Cu-i** (41.9 $kJ mol^{-1}$),[1e] and is comparable to that of **UTSA-74** (31 $kJ mol^{-1}$).[5c] These data indicate **FeNi-M′MOF** has a lower regeneration energy for C_2H_2 production, which would be beneficial for practical applications.

To understand the separation performance of **FeNi-M′MOF**, the adsorption modes of C_2H_2 in **FeNi-M′MOF** were established by DFT-D calculations (see Figure S14). The modeling structures indicated that there are two binding sites for C_2H_2 in **FeNi-M′MOF**: Site I, located in the middle of two adjacent pyz rings, where C_2H_2 was adsorbed through the π–π interactions between C_2H_2 and the pyz rings (see Figure S14a). The C_2H_2 static binding energy in site I is up to 41.4 $kJ mol^{-1}$. Site II, located in the middle of two adjacent Ni open metal sites, where C_2H_2 a molecule is adsorbed through the interactions between C≡C and Ni open metal sites and is perpendicular to *c* axis. The C_2H_2 static binding energy in this site is 29.9 $kJ mol^{-1}$, which is smaller than that of site I (see Figure S14b).

Further visualization of these host–guest interactions was carried out through high-resolution neutron powder diffraction experiments. The crystal structure under low C_2D_2 loading was measured first (Figure 4a). As expected, C_2D_2 molecules preferentially distribute on site I. C_2D_2 molecules were identified between the two pyz rings through π–π stacking (3.552 Å). The C_2D_2 molecules show a titling angle of 27.4° from the [001] direction (crystallographic *c* axis; see Figure S15a). In addition, multiple intermolecular interactions were also observed between C_2D_2 and **FeNi-M′MOF** ($D^{\delta+}\cdots N^{\delta-}$: 2.977 Å, $C^{\delta-}\cdots N^{\delta-}$: 3.808 Å, Figure 4c; see Figure S15b). In contrast, the preferential CO_2 binding site is located at the open Ni site (Figure 4b). The electronegative $O^{\delta-}$ atoms of CO_2 interact with the positive open-metal site $Ni^{\delta+}$. However, the distance across the channel is insufficient

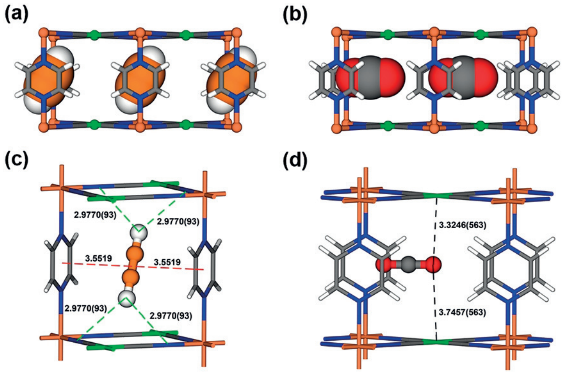

Figure 4. Neutron diffraction crystal structure of a) **FeNi-M′MOF⊃C_2D_2** and b) **FeNi-M′MOF⊃CO_2**, viewed from the *a*/*b* axis. Adsorption binding sites of c) C_2D_2 and c) CO_2 for **FeNi-M′MOF**. Fe, Ni, C, N, O, H in **FeNi-M′MOF** and CO_2 are represented by orange, green, gray, blue, red, and white, respectively; C and D in C_2D_2 are represented by orange and white, respectively. The labelled distance is measured in Å.

for favorable $Ni^{\delta+}\cdots O^{\delta-}{=}C{=}O^{\delta-}\cdots Ni^{\delta+}$ interactions to form in the structure. Thus, CO_2 molecules were adsorbed near the center of the channel and parallel to the channel. $O^{\delta-}$ atom of CO_2 inserts between the adjacent two $Ni^{\delta+}$ atoms from different layers and the distance of $O^{\delta-}\cdots Ni^{\delta+}$ are 3.746 and 3.325 Å, respectively (Figure 4d). This type interaction is relatively weak, consistent with the gentle adsorption isotherm and low Q_{st} value of CO_2 in **FeNi-M′MOF**. The multiple binding sites of **FeNi-M′MOF** for gas molecules and its different binding modes toward C_2H_2 and CO_2 enable **FeNi-M′MOF** to selectively adsorb C_2H_2 from CO_2 with both high C_2H_2 uptake and remarkable C_2H_2/CO_2 selectivity.

In summary, highly selective C_2H_2/CO_2 separation has been successfully realized by a mixed iron/nickel MOF **FeNi-M′MOF** using a metalloligand approach. The structural features the of cyanonickelate and optimal pore channels in this MOF allow C_2H_2 molecules to interact at multiple binding sites, with both very high C_2H_2 uptake and C_2H_2/CO_2 selectivity in volumetric ratio. The so-called dual functionality in this material enables this MOF to serve as one of the best materials for C_2H_2/CO_2 separation in terms of C_2H_2-capture capability. This work also illustrates an outstanding example to further reveal the huge separation potential of MOF adsorbents, especially for challenging gas separation and purification. The active ongoing research affords tremendous opportunities for energy-efficient separation.

Acknowledgements

This work was supported by the Zhejiang Provincial Natural Science Foundation of China (LY20E020001), National Natural Science Foundation of China (51602301 and 51672251), and the Welch Foundation (AX-1730). J.G. acknowledges the Fundamental Research Funds of Zhejiang Sci-Tech University (2019Q007).

Conflict of interest

The authors declare no conflict of interest.

Keywords: acetylene · adsorption · gas separation · iron · metal–organic frameworks

How to cite: *Angew. Chem. Int. Ed.* **2020**, *59*, 4396–4400
Angew. Chem. **2020**, *132*, 4426–4430

---

[1] a) H. Li, L. Li, R.-B. Lin, W. Zhou, S. Xiang, B. Chen, Z. Zhang, *EnergyChem* **2019**, *1*, 100006; b) M. Ding, R. W. Flaig, H.-L. Jiang, O. M. Yaghi, *Chem. Soc. Rev.* **2019**, *48*, 2783–2828; c) R.-B. Lin, L. Li, H.-L. Zhou, H. Wu, C. He, S. Li, R. Krishna, J. Li, W. Zhou, B. Chen, *Nat. Mater.* **2018**, *17*, 1128–1133; d) M. K. Taylor, T. Runčevski, J. Oktawiec, J. E. Bachman, R. L. Siegelman, H. Jiang, J. A. Mason, J. D. Tarver, J. R. Long, *J. Am. Chem. Soc.* **2018**, *140*, 10324–10331; e) X. Cui, K. Chen, H. Xing, Q. Yang, R. Krishna, Z. Bao, H. Wu, W. Zhou, X. Dong, Y. Han, B. Li, Q. Ren, M. J. Zaworotko, B. Chen, *Science* **2016**, *353*, 141–144; f) A. Cadiau, K. Adil, P. M. Bhatt, Y. Belmabkhout, M. Eddaoudi, *Science* **2016**, *353*, 137–140; g) R.-B. Lin, S. Xiang, W. Zhou, B. Chen, *Chem* **2019**, https://doi.org/10.1016/j.chempr.2019.1010.1012.

[2] a) K.-J. Chen, D. G. Madden, S. Mukherjee, T. Pham, K. A. Forrest, A. Kumar, B. Space, J. Kong, Q.-Y. Zhang, M. J. Zaworotko, *Science* **2019**, *366*, 241–246; b) Y. Liu, Z. Chen, G. Liu, Y. Belmabkhout, K. Adil, M. Eddaoudi, W. Koros, *Adv. Mater.* **2019**, *31*, 1807513; c) W. G. Cui, T. L. Hu, X. H. Bu, *Adv. Mater.* **2019**, *31*, 1806445; d) R. L. Siegelman, P. J. Milner, E. J. Kim, S. C. Weston, J. R. Long, *Energy Environ. Sci.* **2019**, *12*, 2161–2173; e) L. Li, R.-B. Lin, R. Krishna, H. Li, S. Xiang, H. Wu, J. Li, W. Zhou, B. Chen, *Science* **2018**, *362*, 443–446; f) P.-Q. Liao, N.-Y. Huang, W.-X. Zhang, J.-P. Zhang, X.-M. Chen, *Science* **2017**, *356*, 1193–1196; g) S. Yang, A. J. Ramirez-Cuesta, R. Newby, V. Garcia-Sakai, P. Manuel, S. K. Callear, S. I. Campbell, C. C. Tang, M. Schröder, *Nat. Chem.* **2014**, *7*, 121–129; h) M. L. Aubrey, M. T. Kapelewski, J. F. Melville, J. Oktawiec, D. Presti, L. Gagliardi, J. R. Long, *J. Am. Chem. Soc.* **2019**, *141*, 5005–5013.

[3] C. R. Reid, K. M. Thomas, *J. Phys. Chem. B* **2001**, *105*, 10619–10629.

[4] a) H. Yang, T. X. Trieu, X. Zhao, Y. Wang, Y. Wang, P. Feng, X. Bu, *Angew. Chem. Int. Ed.* **2019**, *58*, 11757–11762; *Angew. Chem.* **2019**, *131*, 11883–11888; b) J. Lee, C. Y. Chuah, J. Kim, Y. Kim, N. Ko, Y. Seo, K. Kim, T. H. Bae, E. Lee, *Angew. Chem. Int. Ed.* **2018**, *57*, 7869–7873; *Angew. Chem.* **2018**, *130*, 7995–7999; c) R.-B. Lin, L. Li, H. Wu, H. Arman, B. Li, R.-G. Lin, W. Zhou, B. Chen, *J. Am. Chem. Soc.* **2017**, *139*, 8022–8028; d) M. Jiang, X. Cui, L. Yang, Q. Yang, Z. Zhang, Y. Yang, H. Xing, *Chem. Eng. J.* **2018**, *352*, 803–810; e) H. S. Scott, M. Shivanna, A. Bajpai, D. G. Madden, K.-J. Chen, T. Pham, K. A. Forrest, A. Hogan, B. Space, J. J. Perry IV, M. J. Zaworotko, *ACS Appl. Mater. Interfaces* **2017**, *9*, 33395–33400; f) K.-J. Chen, H. S. Scott, D. G. Madden, T. Pham, A. Kumar, A. Bajpai, M. Lusi, K. A. Forrest, B. Space, J. J. Perry IV, M. J. Zaworotko, *Chem* **2016**, *1*, 753–765; g) O. T. Qazvini, R. Babarao, Z.-L. Shi, Y.-B. Zhang, S. G. Telfer, *J. Am. Chem. Soc.* **2019**, *141*, 5014–5020.

[5] a) H. Zeng, M. Xie, Y.-L. Huang, Y. Zhao, X.-J. Xie, J.-P. Bai, M.-Y. Wan, R. Krishna, W. Lu, D. Li, *Angew. Chem. Int. Ed.* **2019**, *58*, 8515–8519; *Angew. Chem.* **2019**, *131*, 8603–8607; b) J. Duan, M. Higuchi, J. Zheng, S.-I. Noro, I.-Y. Chang, K. Hyeon-Deuk, S. Mathew, S. Kusaka, E. Sivaniah, R. Matsuda, *J. Am. Chem. Soc.* **2017**, *139*, 11576–11583; c) F. Luo, C. Yan, L. Dang, R. Krishna, W. Zhou, H. Wu, X. Dong, Y. Han, T.-L. Hu, M. O'Keeffe, L.

Wang, M. Luo, R.-B. Lin, B. Chen, *J. Am. Chem. Soc.* **2016**, *138*, 5678 – 5684.

[6] a) Y.-L. Peng, T. Pham, P. Li, T. Wang, Y. Chen, K.-J. Chen, K. A. Forrest, B. Space, P. Cheng, M. J. Zaworotko, Z. Zhang, *Angew. Chem. Int. Ed.* **2018**, *57*, 10971 – 10975; *Angew. Chem.* **2018**, *130*, 11137 – 11141; b) Y.-P. Li, Y. Wang, Y.-Y. Xue, H.-P. Li, Q.-G. Zhai, S.-N. Li, Y.-C. Jiang, M.-C. Hu, X. Bu, *Angew. Chem. Int. Ed.* **2019**, *58*, 13590 – 13595; *Angew. Chem.* **2019**, *131*, 13724 – 13729; c) Y. Ye, Z. Ma, R.-B. Lin, R. Krishna, W. Zhou, Q. Lin, Z. Zhang, S. Xiang, B. Chen, *J. Am. Chem. Soc.* **2019**, *141*, 4130 – 4136.

[7] a) D. Aguilà, Y. Prado, E. S. Koumousi, C. Mathoniere, R. Clérac, *Chem. Soc. Rev.* **2016**, *45*, 203 – 224; b) M. B. Zakaria, T. Chikyow, *Coord. Chem. Rev.* **2017**, *352*, 328 – 345; c) K. Otsubo, T. Haraguchi, H. Kitagawa, *Coord. Chem. Rev.* **2017**, *346*, 123 – 138; d) S. Sakaida, K. Otsubo, O. Sakata, C. Song, A. Fujiwara, M. Takata, H. Kitagawa, *Nat. Chem.* **2016**, *8*, 377 – 383; e) M. M. Deshmukh, M. Ohba, S. Kitagawa, S. Sakaki, *J. Am. Chem. Soc.* **2013**, *135*, 4840 – 4849; f) J. T. Culp, M. R. Smith, E. Bittner, B. Bockrath, *J. Am. Chem. Soc.* **2008**, *130*, 12427 – 12434.

[8] a) M. C. Das, S. Xiang, Z. Zhang, B. Chen, *Angew. Chem. Int. Ed.* **2011**, *50*, 10510 – 10520; *Angew. Chem.* **2011**, *123*, 10696 – 10707; b) S.-C. Xiang, Z. Zhang, C.-G. Zhao, K. Hong, X. Zhao, D.-R. Ding, M.-H. Xie, C.-D. Wu, M. C. Das, R. Gill, K. Tomas, B. Chen, *Nat. Commun.* **2011**, *2*, 204.

[9] V. Niel, J. M. Martinez-Agudo, M. C. Muñoz, A. B. Gaspar, J. A. Real, *Inorg. Chem.* **2001**, *40*, 3838 – 3839.

[10] J. Gao, J. Cong, Y. Wu, L. Sun, J. Yao, B. Chen, *ACS Appl. Energy Mater.* **2018**, *1*, 5140 – 5144.

[11] X. Duan, Q. Zhang, J. Cai, Y. Yang, Y. Cui, Y. He, C. Wu, R. Krishna, B. Chen, G. Qian, *J. Mater. Chem. A* **2014**, *2*, 2628 – 2633.

[12] J. Duan, W. Jin, R. Krishna, *Inorg. Chem.* **2015**, *54*, 4279 – 4284.

[13] S. Xiang, W. Zhou, Z. Zhang, M. A. Green, Y. Liu, B. Chen, *Angew. Chem. Int. Ed.* **2010**, *49*, 4615 – 4618; *Angew. Chem.* **2010**, *122*, 4719 – 4722.

[14] P. Li, Y. He, Y. Zhao, L. Weng, H. Wang, R. Krishna, H. Wu, W. Zhou, M. O'Keeffe, Y. Han, B. Chen, *Angew. Chem. Int. Ed.* **2015**, *54*, 574 – 577; *Angew. Chem.* **2015**, *127*, 584 – 587.

[15] Y. He, R. Krishna, B. Chen, *Energy Environ. Sci.* **2012**, *5*, 9107 – 9120.

[16] E. D. Bloch, W. L. Queen, R. Krishna, J. M. Zadrozny, C. M. Brown, J. R. Long, *Science* **2012**, *335*, 1606 – 1610.

Manuscript received: January 7, 2020
Accepted manuscript online: January 13, 2020
Version of record online: January 30, 2020

Angewandte Chemie
Eine Zeitschrift der Gesellschaft Deutscher Chemiker

Supporting Information

Mixed Metal–Organic Framework with Multiple Binding Sites for Efficient C_2H_2/CO_2 Separation

Junkuo Gao, Xuefeng Qian, Rui-Biao Lin,* Rajamani Krishna, Hui Wu, Wei Zhou,* and Banglin Chen**

anie_202000323_sm_miscellaneous_information.pdf

1. Materials and general methods

All chemicals were purchased from Alfa Aesar, TCI chemical and Aldrich and used without further purification. Powder X-ray diffraction data were recorded on a Bruker D8 Advance diffractometer with a graphite-monochromatized Cu Ka radiation. The gas sorption isotherms were collected using an automatic volumetric adsorption apparatus Micromeritics ASAP 2020. The specific surface areas of sample were measured with a N_2 adsorption-desorption isotherms by the Brunauer-Emmett-Teller (BET) method at 77 K. All the samples were degassed at 100 ℃ for 3 hours before the gas sorption measurements. Thermogravimetric analysis (TGA) was carried out under air atmosphere from room temperature to 500 °C using a Shimadzu TGA-50 analyzer at a heating rate of 10 °C min^{-1}. For variable-temperature powder X-ray diffraction (VT-PXRD), the measured parameter included a scan speed of 10 ° min^{-1}, a step size of 0.02° and a scan range of 2θ from 10° to 40°. The heating rate is 5 ℃ min^{-1} and the sample was maintained 5 minutes at each target temperature. The target temperatures are set as follows: 60 ℃, 90 ℃, 120 ℃, 150 ℃, 180 ℃ and 200 ℃. The energy-dispersive X-ray spectroscopy (EDS) analyses were carried out by transmission electron microscopy (TEM, JEM-2100).

2. Synthesis of [Fe(pyz)Ni(CN)$_4$] (FeM-M'MOF)

$Fe(ClO_4)_2\cdot xH_2O$ (1 mmol) and pyrazine (1 mmol) were dissolved in a mixture of 50 ml of deionized water and 50 ml of methanol under the protection of N_2. **Caution! Iron (II) perchlorate salt is potentially explosive and must be handled with care!** Separately, 1 mmol of $K_2[M(CN)_4]$ (M = Ni, Pt) is dissolved in 20 ml of deionized water and the solution is dropwise added to the $Fe(ClO_4)_2\cdot xH_2O$-pyrazine solution. Precipitation of the clathrates instantaneously occurs under vigorous stirring. After stirring for 30 minutes, separated by Centrifuge the powder was recovered and washed with water several times, then dry in vacuum overnight at room temperature. Elemental analysis of activated **FeNi-M’MOF** ($C_8H_4N_6FeNi$), Calcd: C. 32.17%; H, 1.35%; N, 28.14% and found: C, 32.45%; H, 1.64%; N, 28.36%.

3. Fitting of pure component isotherms

The experimentally measured loadings for C_2H_2, and CO_2 at 273 K, and 298 K in **FeM-M'MOF** were fitted with the dual-Langmuir isotherm model

$$q = q_{A,sat}\frac{b_A p}{1+b_A p} + q_{B,sat}\frac{b_B p}{1+b_B p} \quad (1)$$

The Langmuir parameters for each site is temperature-dependent

$$b_A = b_{A0}\exp\left(\frac{E_A}{RT}\right); \quad b_b = b_{B0}\exp\left(\frac{E_B}{RT}\right) \quad (2)$$

The Dual-site Langmuir fit parameters are provided in Table S3 and S4.

4. Isosteric heat of adsorption

The binding energy of C_2H_2 is reflected in the isosteric heat of adsorption, Q_{st}, defined as

$$Q_{st} = RT^2\left(\frac{\partial \ln p}{\partial T}\right)_q \quad (3)$$

5. IAST calculations of adsorption selectivities

In order to compare the C_2H_2/CO_2 separation performance of various MOFs, IAST calculations of mixture adsorption were performed. For separation of a binary mixture of components A and B, the adsorption selectivity is defined by

$$S_{ads} = \frac{q_A/q_B}{y_A/y_B} \quad (4)$$

where the q_A, and q_B represent the molar loadings, expressed in mol kg^{-1}, within the MOF that is in equilibrium with a bulk fluid mixture with mole fractions y_A, and $y_B = 1 - y_A$. The molar loadings, also called *gravimetric uptake capacities*, are usually expressed with the units mol kg^{-1}. The IAST calculations of 50/50 mixture adsorption taking the mole fractions $y_A = 0.5$ and $y_B = 1 - y_A = 0.5$ for a range of pressures up to 100 kPa and 298 K were performed.

6. Transient breakthrough simulations

The performance of industrial fixed bed adsorbers is dictated by a combination of adsorption selectivity and uptake capacity. For a proper comparison of various MOFs, we perform transient breakthrough simulations using the simulation methodology described in the literature.[S1] or the breakthrough simulations, the following parameter values were used: length of packed bed, L = 0.3 m; voidage of packed bed, $\varepsilon = 0.4$; superficial gas velocity at inlet, $u = 0.04$ m/s. The transient breakthrough simulation results are presented in terms of a *dimensionless* time, τ, defined as $\tau = \frac{tu}{\varepsilon L}$.

During the initial transience, the effluent gas contains pure CO_2 and this continues until C_2H_2 starts breaking through because its uptake capacity in the MOF has been reached.

During a certain time interval, $\Delta\tau$, pure CO_2 can be recovered in the gas phase. As in previous works,[S1a] we set the purity of CO_2 to 99.95%. The MOFs are all compared on the basis of the moles of 99.95% pure CO_2 produced per L of adsorbent material.

If τ_{break} is the breakthrough time for C_2H_2, during the time interval 0 to τ_{break}, C_2H_2 is captured. The volumetric C_2H_2 capture capacity, expressed in mol/L, can be determined from a material balance.

7. Neutron diffraction experiment

Neutron powder diffraction (NPD) measurements were conducted using the BT-1 neutron powder diffractometer at the National Institute of Standards and Technology (NIST) Center for Neutron Research. A Ge(311) monochromator with a 75° take-off angle, λ = 2.0787(2) Å, and in-pile collimation of 60 minutes of *arc* was used. Data were collected over the range of 1.3-166.3° (2θ) with a step size of 0.05°. Fully activated **FeNi-M'MOF** sample was loaded in a vanadium can equipped with a capillary gas line. A closed-cycle He refrigerator was used to control the sample temperature. The bare MOF sample was measured first. To investigate the gas adsorption structure, the sample was charged with gas molecules at pre-determined pressures and temperatures, and allowed enough time to reach equilibrium. Diffraction data were then collected on the gas-loaded samples. For comparison purpose, both CO_2 and C_2D_2 were studied. Note that for acetylene adsorption, deuterated gas C_2D_2 was used to avoid the large incoherent neutron scattering background that would be produced by the hydrogen in C_2H_2. Rietveld structural refinement was performed on the neutron diffraction data using the GSAS package. Due to the large number of atoms in the crystal unit cell, the ligand molecule and the gas molecule were both treated as rigid bodies in the Rietveld refinement (to limit the number of variables), with the molecule orientation and center of mass freely refined. Final refinement on lattice parameters, atomic coordinates, positions/orientations of the rigid bodies, thermal factors, gas molecule occupancies, background, and profiles all converge with satisfactory R-factors.

8. Breakthrough experiments

The breakthrough experiments were carried out in dynamic gas breakthrough set-up. A stainless-steel column with inner dimensions of 4 × 150 mm was used for sample packing. MOF particles (0.560 g) with size of 220-320 μm obtained through particle size sieving was then packed into the column. The column was placed in a temperature-controlled environment (maintained at 298 K). The mixed gas flow and pressure were controlled by using a pressure controller valve and a mass flow controller (Figure S1). Outlet effluent from the column was continuously monitored using gas chromatography (GC-2014, SHIMADZU) with a thermal conductivity detector (TCD, detection limit 0.1 ppm). The column packed with sample was firstly purged with He flow (100 mL $\min^{-1}$) for 6 h at room temperature 298 K. The mixed gas flow rate during breakthrough process is 2 mL $\min^{-1}$ using 50/50 (v/v) C_2H_2/CO_2. After the breakthrough experiment, the sample was regenerated under vacuum.

The actual C_2H_2 capture amount and separation factor of C_2H_2/CO_2 were calculated by reported method.[S2] The actual adsorbed amount of gas i (q_i) is calculated from the breakthrough curve by the equation:

$$q_i = \frac{F_i \times t_0 - V_{dead} - \int_0^{t_0} F_e \Delta t}{m} \tag{5}$$

where F_i is the influent flow rate of the specific gas (ml $\min^{-1}$); t_0 is the adsorption time (min); V_{dead} is the dead volume of the system (cm^3); F_e is the effluent flow rate of the specific gas (ml $\min^{-1}$); and m is the mass of the sorbent (g). The separation factor (α) of the breakthrough experiment is determined as

$$\alpha = \frac{q_1}{q_2} \times \frac{y_2}{y_1} \tag{6}$$

where y_i is the molar fraction of gas i in the gas mixture.

In this case, the adsorbed amounts of C_2H_2 are calculated to be 4.10 mol L^{-1}. Accordingly, the separation factor is $\alpha = 1.7$.

Table S1. Crystallographic Data of **FeNi-M'MOF**, **FeNi-M'MOF⊃C_2D_2** and **FeNi-M'MOF⊃CO_2**.

Compound name	**FeNi-M'MOF**	**FeNi-M'MOF⊃C_2D_2**	**FeNi-M'MOF⊃CO_2**
CCDC	1958795	1958796	1958797
Empirical formula	$C_8H_4N_6FeNi$	$C_{9.39}H_4D_{1.39}N_6FeNi$	$C_{8.71}H_4N_6O_{1.41}FeNi$
Formula weight	298.70	318.16	329.81
Crystal system	Tetragonal	Tetragonal	Tetragonal
Space group	P4/mmm	P 4/mmm	P4/mmm
a (Å)	7.1535(10)	7.1038(9)	7.1590(10)
b (Å)	7.1535	7.1038	7.159
c (Å)	7.0515(16)	6.9381(16)	7.0440(14)
α (°)	90	90.0	90.0
β (°)	90	90.0	90.0
γ (°)	90	90.0	90.0
Volume ($Å^3$)	360.843	350.124	361.014
Z	1	1	1
R_p[a]$I>2\Theta$	0.0195	0.0169	0.0179
R_{wp}[b]$I>2\Theta$	0.0242	0.0208	0.0220

[a] $R_p = \Sigma|cY^{sim}(2\theta_i) - I^{exp}(2\theta_i) + Y^{back}(2\theta_i)|/\Sigma|I^{exp}(2\theta_i)|$.

[b] $R_{wp} = \{w_p[cY^{sim}(2\theta_i) - I^{exp}(2\theta_i) + Y^{back}(2\theta_i)]2/\Sigma w_p[I^{exp}(2\theta_i)]2\}^{1/2}$, and $w_p = 1/I^{exp}(2\theta_i)$.

Table S2. Comparisons of the density of accessible metal sites between **FeNi-M'MOF** and other MOFs.

MOF	Formula	Formula Weight (g mol^{-1})	Density (g cm^{-3})	Volumetric density of accessible metal sites (mmol cm^{-3})
Zn-MOF-74	$Zn_2C_8H_2O_6$	324.88	1.219	7.5[S3]
Co-MOF-74	$Co_2C_8H_2O_6$	311.96	1.181	7.6[S4]
Ni-MOF-74	$Ni_2C_8H_2O_6$	311.48	1.194	7.7[S5]
PCP-31	$Cu_2C_{22}H_{12}O_{10}$	563.40	0.703	2.5[S6]
HKUST-1	$Cu_3C_{18}H_6O_{12}$	604.87	0.879	4.4[S7]
Ni-(*m*-dobdc)	$Ni_2C_8H_2O_6$	311.48	1.200	7.7[S8]
UTSA-74a*	$Zn_2C_8H_2O_6$	324.88	1.342	8.3[S9]
FeNi-M'MOF*	$FeNiC_8H_4N_6$	298.70	1.375	**9.2** (this work)

*Noted that every open metal center in these MOFs have two accessible sites.

Table S3. Dual-site Langmuir fit parameters for C_2H_2, and CO_2 in **FeNi-M'MOF** at 298 K.

	Site A			Site B		
	$q_{A,sat}$ mol kg^{-1}	b_{A0} Pa^{-1}	E_A kJ mol^{-1}	$q_{B,sat}$ mol kg^{-1}	b_{B0} Pa^{-1}	E_B kJ mol^{-1}
C_2H_2	1	4.18E-13	40	4.1	7.70E-9	27
CO_2	3.84	9.46E-10	25			

Table S4. Dual-site Langmuir fit parameters for C_2H_2, and CO_2 in **FePt-M'MOF** at 298 K.

	Site A			Site B		
	$q_{A,sat}$ mol kg^{-1}	b_{A0} Pa^{-1}	E_A kJ mol^{-1}	$q_{B,sat}$ mol kg^{-1}	b_{B0} Pa^{-1}	E_B kJ mol^{-1}
C_2H_2	2.3	1.01E-09	31	0.9	1.49E-11	30
CO_2	2.8	2.06E-10	29			

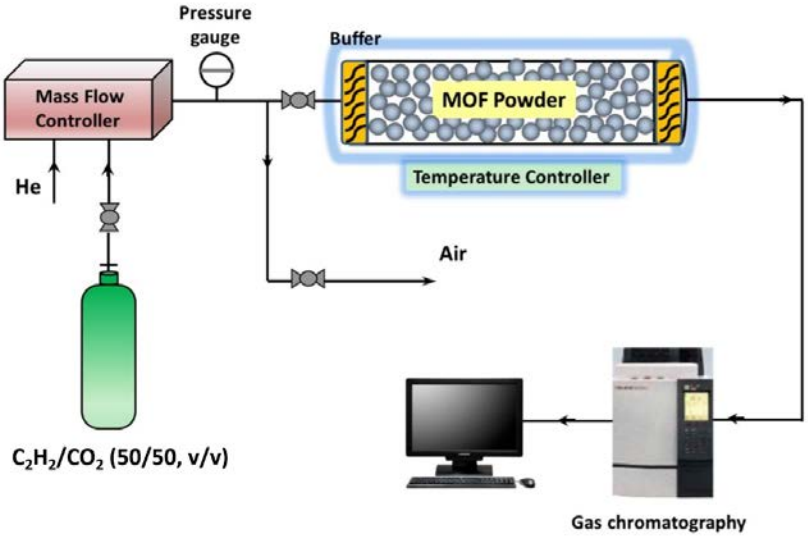

Figure S1. Illustration of the self-built breakthrough apparatus.

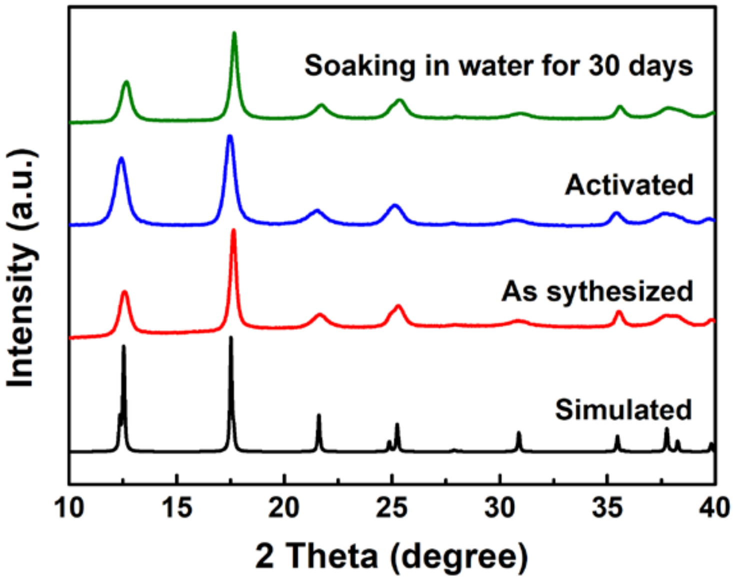

Figure S2. Powder X-ray diffraction patterns of FeNi-M'MOF at different conditions.

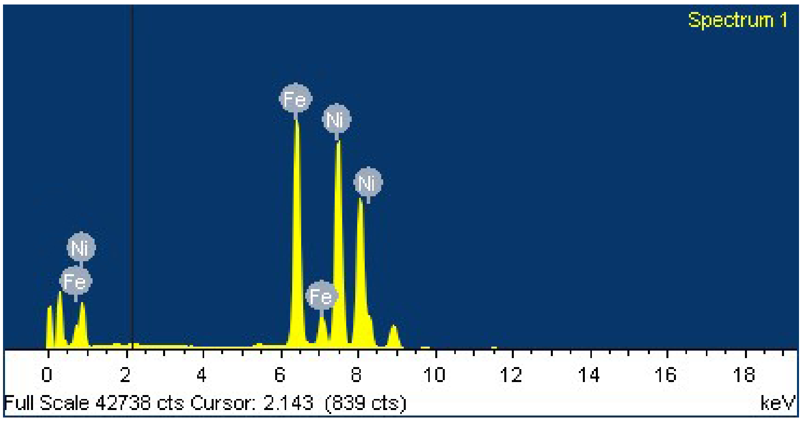

Figure S3. EDS spectra of **FeNi-M'MOF**. The atomic molar ratio of Fe/Ni is 1.07, which is almost identical with the theoretical ratio of 1 in **FeNi-M'MOF**.

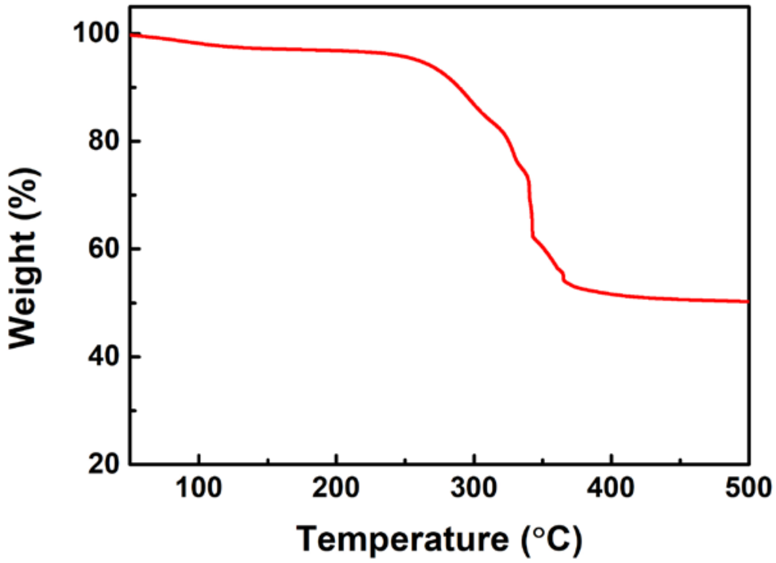

Figure S4. TGA curve of **FeNi-M'MOF** under air atmosphere.

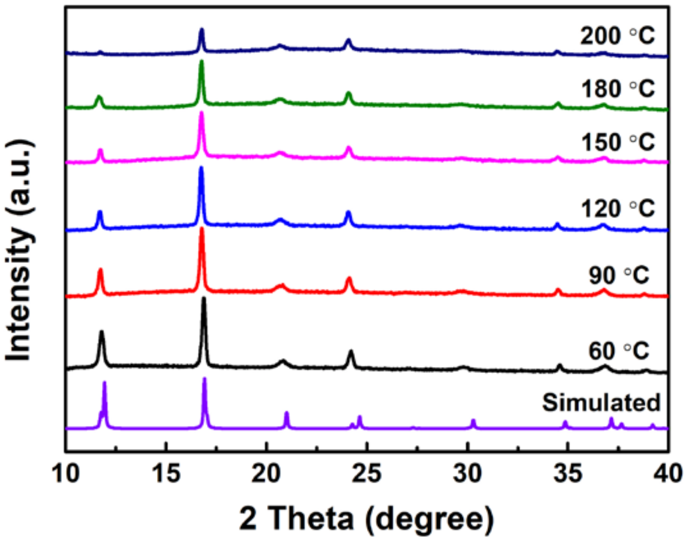

Figure S5. Variable-temperature PXRD patterns of FeNi-M'MOF under air atmosphere.

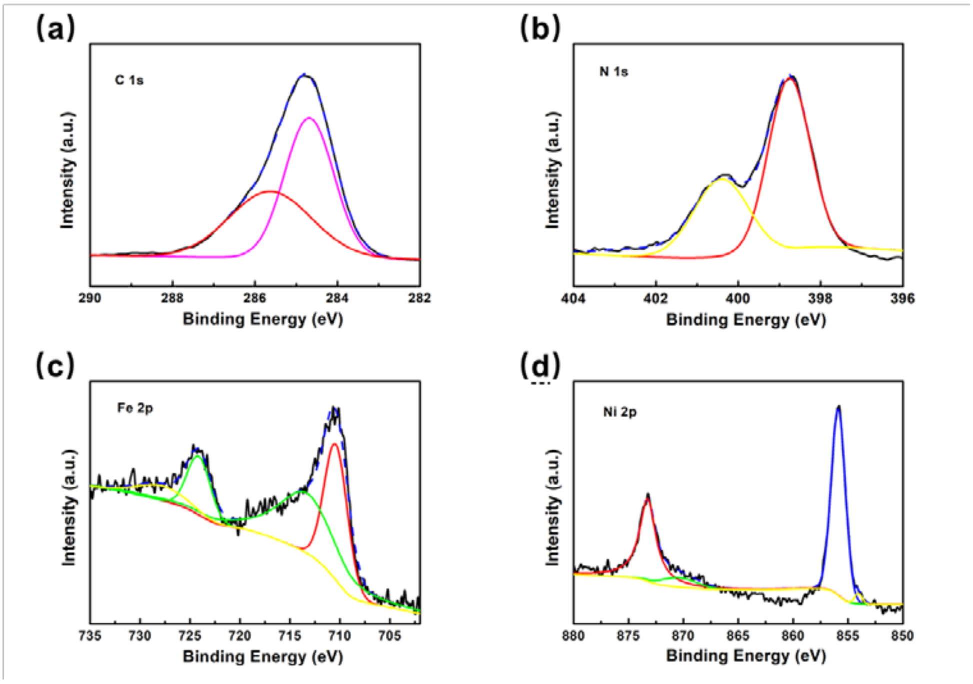

Figure S6. XPS spectra of **FeNi-M'MOF**. C 1s spectra (a), N 1s spectra (b), Fe 2p spectra (c) and Ni 2p spectra (d) of **FeNi-M'MOF**. The binding energies of Fe $2p_{3/2}$, $2P_{1/2}$ and satellite in **FeNi-M'MOF** are recorded at approximately 710.41 eV, 713.98 eV and 724.13 eV, which correspond to Fe^{2+}.[S10] The binding energies of Ni $2p_{3/2}$ and $2P_{1/2}$ in **FeNi-M'MOF** are recorded at approximately 855.8 eV and 873.28 eV, which correspond to Ni^{2+}.[S11] The molar ratio of Fe/Ni in **FeNi-M'MOF** is 1.03 based on XPS data, which is almost identical with the theoretical ratio of 1.

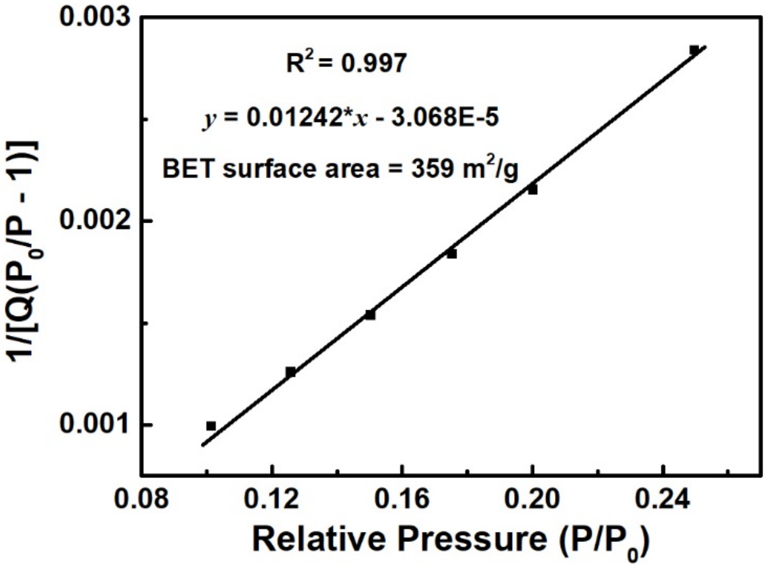

Figure S7. Calculation of BET surface area for **FeNi-M'MOF** based on N_2 adsorption isotherm at 77 K.

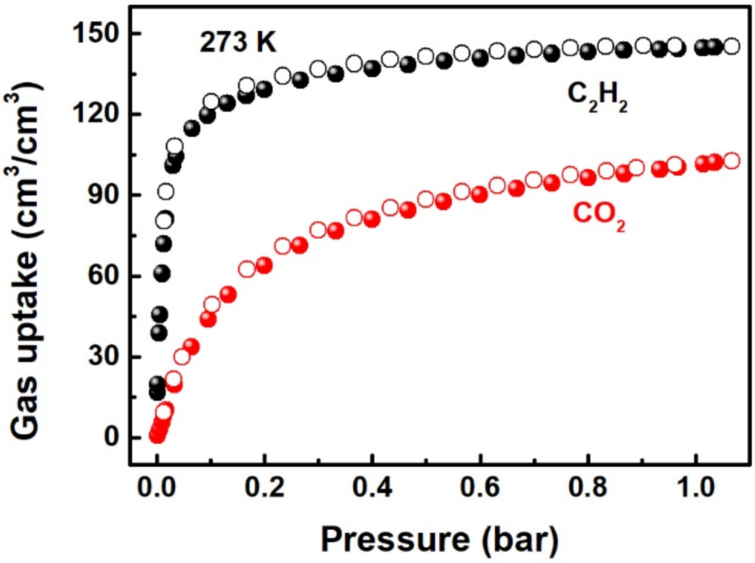

Figure S8. Single-component adsorption (solid) and desorption (open) isotherms of C_2H_2 and CO_2 in **FeNi-M'MOF** at 273 K.

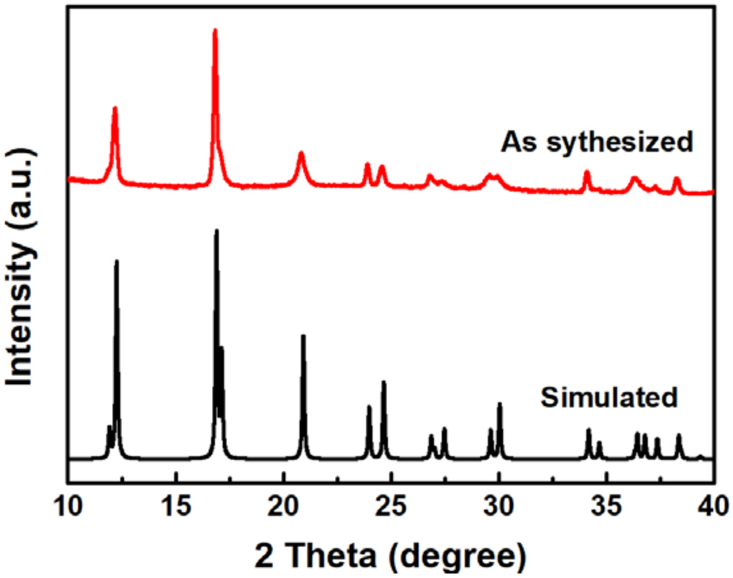

Figure S9. PXRD of simulated **FePt-M'MOF** and as synthesized **FePt-M'MOF**.

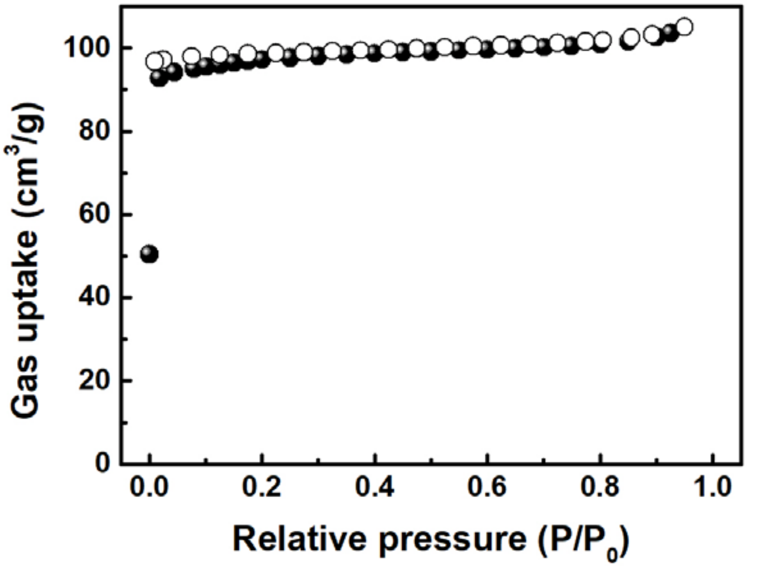

Figure S10. N_2 sorption isotherms for **FePt-M'MOF** at 77 K.

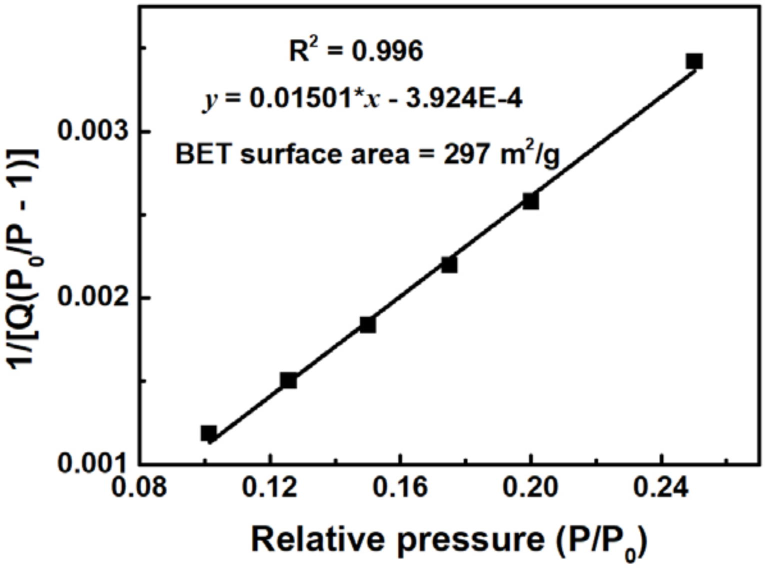

Figure S11. Calculation of BET surface area for **FePt-M'MOF** based on N_2 adsorption isotherm at 77 K.

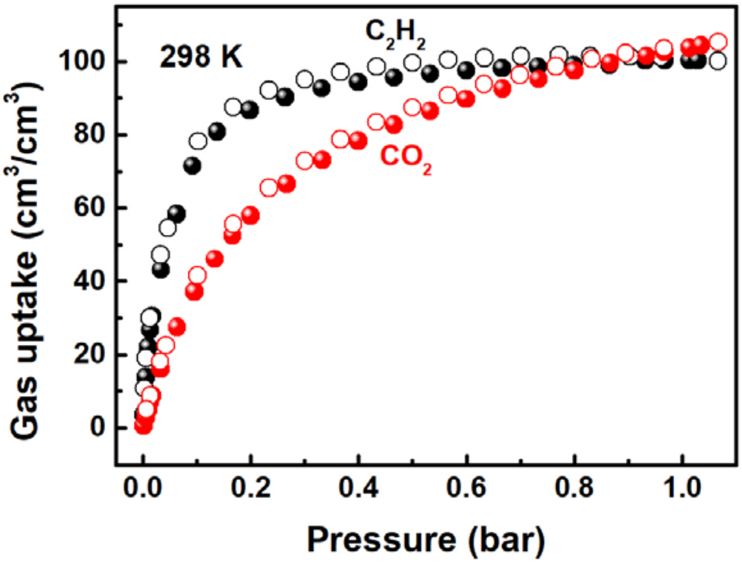

Figure S12. Single-component adsorption (solid) and desorption (open) isotherms of C_2H_2 and CO_2 in **FePt-M'MOF** at 298 K.

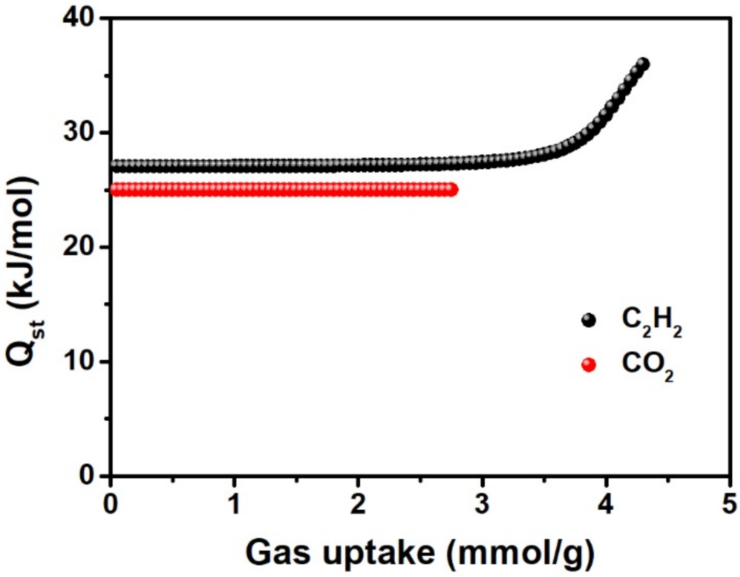

Figure S13. Heats of adsorption of both C_2H_2 and CO_2 in **FeNi-M'MOF**.

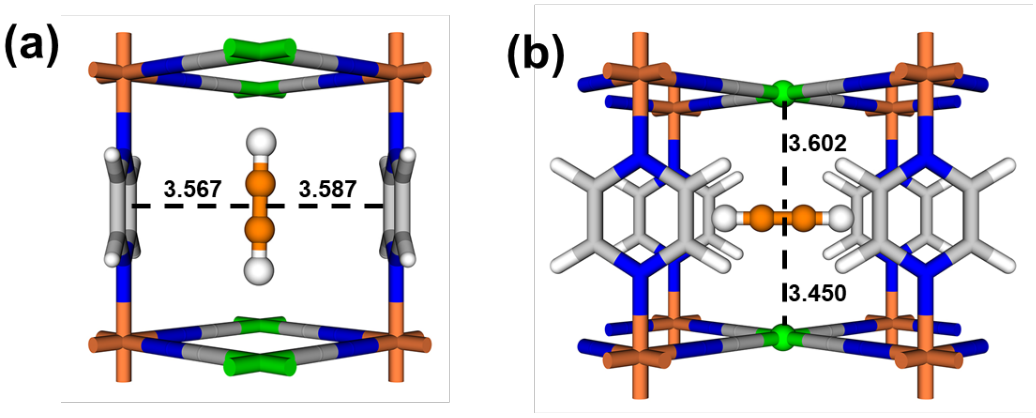

Figure S14. The DFT-D calculations binding sites of C_2H_2 in **FeNi-M'MOF**. Viewed from a/b axis (a) of site I, viewed from a/b axis (b) of site II of C_2H_2. The calculated C_2H_2 static binding energies are 41.4 kJ mol^{-1} on site I and 29.9 kJ mol^{-1} on site II. Fe, Ni, C, N, H in **FeNi-M'MOF** are represented by orange, green, gray, blue and white, respectively; C and H in C_2H_2 are represented by orange and white, respectively. The unit of the distance is Å.

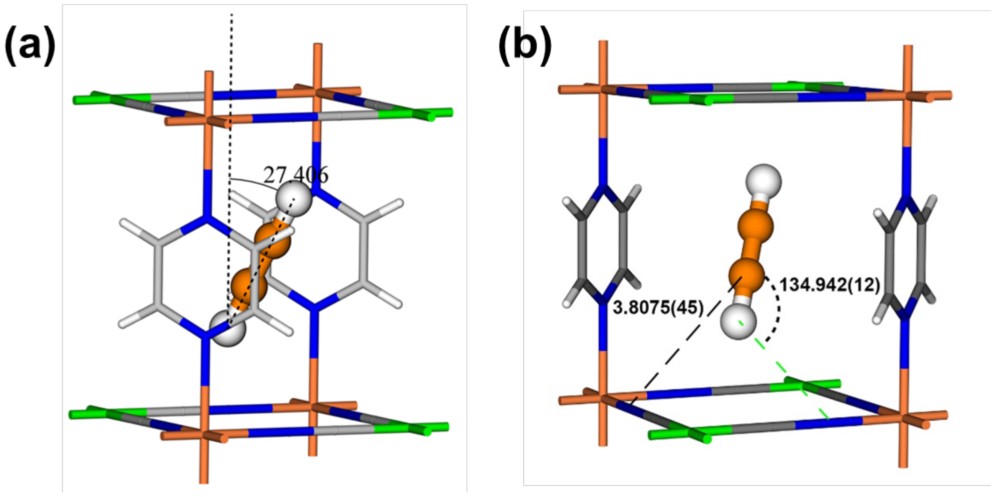

Figure S15. The $C^{\delta-}\cdots N^{\delta-}$ distances and bond angle of the $C\text{-}D^{\delta+}\cdots N^{\delta-}$ between C_2D_2 and **FeNi-M'MOF**. Fe, Ni, C, N, H in **FeNi-M'MOF** are represented by orange, green, gray, blue and white, respectively; C and D in C_2D_2 are represented by orange and white, respectively. The unit of the distance is Å.

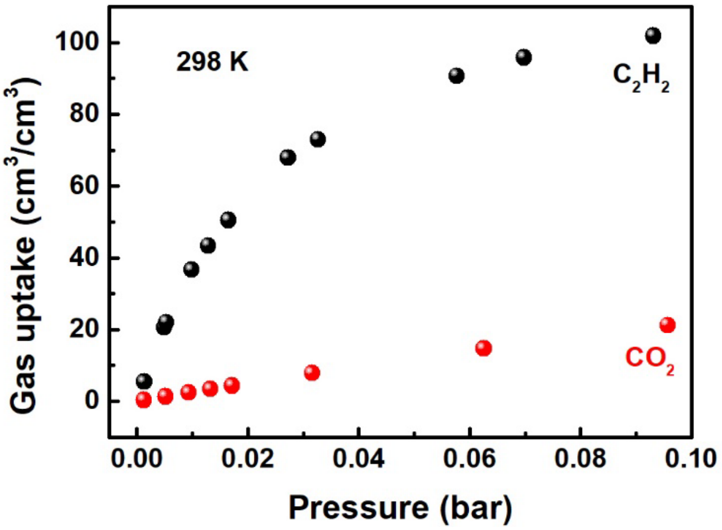

Figure S16. C_2H_2 and CO_2 single-component adsorption isotherms for **FeNi-M'MOF** at 298 K under low pressure (0~0.1 bar).

References

[S1] a) R. Krishna, *RSC Adv.* **2017**, *7*, 35724-35737; b) R. Krishna, *RSC Adv.* **2015**, *5*, 52269-52295.

[S2] P. Li, Y. He, Y. Zhao, L. Weng, H. Wang, R. Krishna, H. Wu, W. Zhou, M. O'Keeffe, Y. Han, B. Chen, *Angew. Chem. Int. Ed.* **2015**, *54*, 574-577.

[S3] N. L. Rosi, J. Kim, M. Eddaoudi, B. Chen, M. O'Keeffe, O. M. Yaghi, *J. Am. Chem. Soc.* **2005**, *127*, 1504-1518.

[S4] P. D. C. Dietzel, Y. Morita, R. Blom, H. Fjellvåg, *Angew. Chem. Int. Ed.* **2005**, *44*, 6354-6358.

[S5] P. D. C. Dietzel, B. Panella, M. Hirscher, R. Blom, H. Fjellvåg, *Chem. Commun.* **2006**, 959-961.

[S6] J. Duan, M. Higuchi, J. Zheng, S.-i. Noro, I. Y. Chang, K. Hyeon-Deuk, S. Mathew, S. Kusaka, E. Sivaniah, R. Matsuda, S. Sakaki, S. Kitagawa, *J. Am. Chem. Soc.* **2017**, *139*, 11576-11583.

[S7] S. S. Y. Chui, S. M. F. Lo, J. P. H. Charmant, A. G. Orpen, I. D. Williams, *Science* **1999**, *283*, 1148-1150.

[S8] M. T. Kapelewski, S. J. Geier, M. R. Hudson, D. Stück, J. A. Mason, J. N. Nelson, D. J. Xiao, Z. Hulvey, E. Gilmour, S. A. FitzGerald, M. Head-Gordon, C. M. Brown, J. R. Long, *J. Am. Chem. Soc.* **2014**, *136*, 12119-12129.

[S9] F. Luo, C. Yan, L. Dang, R. Krishna, W. Zhou, H. Wu, X. Dong, Y. Han, T.-L. Hu, M. O’Keeffe, L. Wang, M. Luo, R.-B. Lin, B. Chen, *J. Am. Chem. Soc.* **2016**, *138*, 5678-5684.

[S10] T. Yamashita, P. Hayes, *Appl. Surf. Sci.* **2008**, *254*, 2441-2449.

[S11] D. Yan, C. Yu, D. Li, X. Zhang, J. Li, T. Lu, L. Pan, *J. Mater. Chem. A* **2016**, *4*, 11077-11085.